



H₂O₂-catalyzed Defluorination of Perfluorooctanesulfonate (PFOS) by Oxidized Vanadium Carbide MXene Nanosheets

Journal:	<i>Journal of Materials Chemistry A</i>
Manuscript ID	TA-ART-04-2023-002073.R2
Article Type:	Paper
Date Submitted by the Author:	13-Jul-2023
Complete List of Authors:	Ye, Yuemei; University of Washington, Civil & Environmental Engineering ; North Carolina State University at Raleigh, Civil, Construction and Environmental Engineering Bang, Hojeong ; University of Washington, Civil & Environmental Engineering Jones, Vivian ; University of Washington, Chemical Engineering Dennehy, Kaylie ; University of Washington, Civil & Environmental Engineering Steigerwald, Jessica ; University of Washington, Civil & Environmental Engineering Ray, Jessica; University of Washington, Civil & Environmental Engineering

H₂O₂-catalyzed Defluorination of Perfluorooctanesulfonate (PFOS) by Oxidized Vanadium Carbide MXene Nanosheets

Yuemei Ye^{a,§}, Jessica M. Steigerwald^a, Hojeong Bang^a, Vivian Jones^b, Kaylie Dennehy^a, and Jessica R. Ray^{a,*}

Received 00th January 20xx,
Accepted 00th January 20xx

DOI: 10.1039/x0xx00000x

Perfluorooctanesulfonate (PFOS) is a fluorinated synthetic surfactant in consumer end products that has been heavily investigated due to its global distribution, environmental persistence, and toxicity. Reductive processes that generate highly reactive reducing species called solvated electrons in water can destroy PFOS C–F bonds. However, solvated electrons are easily scavenged, which results in slow, incomplete defluorination. Heterogeneous catalysts may amplify PFOS defluorination, but the number of suitable catalysts for this process is limited. In this study, we examined PFOS defluorination by oxidized vanadium carbide (V₂C) MXene nanosheets in the presence of hydrogen peroxide (H₂O₂) under room temperature, ambient and aerobic conditions. 96% removal of 50 µg/L PFOS was observed within 4 h by 0.15 mg/mL V(V)-C nanosheets and 14.7 mM H₂O₂ compared to reaction systems containing only V(V)-C (62% removal) or H₂O₂ (no removal) in batch studies. And near-complete (105 ± 23%) defluorination of PFOS after four hours in this V(V)-C-H₂O₂ system following the formation and removal of trifluoroacetic acid—a short-chain degradation product. Solvated electrons (catalyzed by H₂O₂ addition) were hypothesized to contribute to the rapid defluorination of PFOS adsorbed to the V(V)-C surface. Our findings of V(V)-C-catalyzed reductive defluorination of PFOS could be applied to the treatment of other recalcitrant trace organic compounds in impacted water sources.

Introduction

Per- and polyfluoroalkyl substances (PFAS) are a particularly recalcitrant class of synthetic organic compounds broadly used in industrial and consumer products due to their water-resistant and fire-extinguishing properties achieved via the high thermal stability of their characteristic C–F bonds.¹ The production and use of PFAS have resulted in widespread environmental contamination of water sources, which is concerning due to its demonstrated toxicity in humans and animals.^{2–7} Perfluorooctanesulfonate (PFOS) is one of the most stable⁸ and frequently detected PFAS in the environment despite its banned use in 2009 by the United States.^{9–11} Due to their stable C–F bonds, degradation of PFOS is still a major challenge.

Solvated electrons are highly reactive reducing species (standard reduction potential, E°: -2.9 V)¹² capable of cleaving PFAS C–F bonds (E°: -2.7 V).¹³ They are generated when an excess electron is introduced into liquid water,¹ and are proposed to undergo nucleophilic attack on the PFOS electropositive carbon to initiate defluorination. The resulting short-lived carbanion decays into a

halogenated carbon radical (e.g., fluorocarbon) and a halide ion to facilitate degradation and defluorination.¹⁴ Solvated electrons can be generated in solution via excitation of chemical mediators such as sulfite, iodide, and indole acetic acid by low wavelength energy sources (e.g., ultraviolet (UV) light) to attack PFAS in water.^{15,16–18} In addition to chemical addition, high energy inputs and specific aqueous conditions (e.g., alkaline pH, anoxic)^{15,16} are required to mitigate the scavenging of solvated electrons.

Heterogeneous substrates¹⁹ can enhance solvated electron treatment efficacy by localizing PFAS to substrate surfaces during the heterogeneous catalytic reaction.²⁰ Large surface areas may provide a vehicle for compound adsorption and delivery of reactive species to accelerate energy and electron transfer between the nanomaterial and compound in water.²¹ For example, Tian et al. observed > 99% defluorination of 10 mg/L PFOA adsorbed onto organo-modified clay nanoparticle surfaces¹ due to effective delivery of solvated electrons to nearby PFOA on the clay surface.^{1,22,23} Most nanomaterial-facilitated reductive defluorination of PFAS require continuous energy inputs (e.g., UV light or applied electrochemical potential) and/or specific aqueous conditions (e.g., anoxic), which are impractical for large-scale water treatment—particularly for decentralized water treatment. Therefore, it is desirable to develop a heterogeneous catalyst capable of destroying PFAS under milder operating conditions without sacrificing defluorination efficiency.

MXenes are two-dimensional, layered metal carbide or nitride nanomaterials widely used for electrochemical applications^{24,25} because of their excellent electronic conversion capabilities.²⁶ Recently, MXenes have gained attention as catalysts for the

^a Department of Civil & Environmental Engineering, University of Washington, Seattle, Washington 98195-2700 USA. Fax: (206) 543-1543, Tel: (206) 221-0791, E-mail: jessray@uw.edu, <https://ray-aimslab.com/>.

^b Department of Chemical Engineering, University of Washington, Seattle, Washington 98195-2700 USA.

Electronic Supplementary Information (ESI) available: See

DOI: 10.1039/x0xx00000x.

Current address: Construction, Civil and Environmental Engineering Department, North Carolina State University, Raleigh, NC 27606.

reductive transformation of contaminants in water. For example, Pandey et al. demonstrated selective and high-capacity reduction of bromate to bromide in drinking water using Ti_3C_2 nanosheets in which Ti(II) oxidation to Ti(IV) facilitated reduction.²⁷ MXenes were also found to participate in radical-initiating behavior during polymerization,^{28–30} which suggests the strong electron transfer ability in MXenes that could be leveraged for catalyzing redox processes during water treatment. The high adsorption capacities, multivalent states and reactivities, and excellent electron transfer kinetics²⁴ of MXenes could contribute to catalytic organic contaminant transformation.³¹ Vanadium carbide (V_2C) is an under-explored MXene for water treatment despite demonstrated evidence of greater redox reactivity. Vanadium oxide surfaces could enable pseudocapacitive (i.e., reversible redox behavior^{24,32,33}) for high-rate energy storage³⁴ to amplify advanced redox process efficacy at the vanadium surface.^{32,33,35} Therefore, vanadium reactivity coupled with the rapid charge transfer kinetics of MXenes could be exploited to enhance the degradation of recalcitrant chemicals.

In this study, we report a novel catalytic approach for PFOS destruction that leverages the redox reactivity of vanadium, large nanosheet surface area, and advantageous electrochemical properties of MXenes for rapid, catalytic reductive defluorination. The ability of oxidized V_2C nanosheets to degrade PFAS was verified, and proposed mechanisms for PFOS degradation and defluorination with this system were explored and discussed. Degradation of PFOS was examined under aerobic conditions in ultrapure water in the presence of hydrogen peroxide (H_2O_2)—a common disinfectant used in water treatment⁴⁴—which was added to catalyze electron shuttling and reactive species formation in the oxidized V_2C nanosheets. The characterized V_2C nanosheet solution was observed to be hydrolyzed to form a vanadium oxide/carbon composite heterostructure (so called V(V)-C). The as-prepared V(V)-C nanosheets are hypothesized to undergo electron transfer from the carbon to V(V) surface phases which may generate reactive species. The large V(V)-C nanosheet surface area and hydrophobic interactions with –F edge groups generated during V(V)-C synthesis facilitated adsorption of PFOS (a representative PFAS). Electron paramagnetic resonance was used to identify the reactive (oxygen) species responsible for PFOS degradation near V(V)-C nanosheets. Complementary analyses of the aqueous chemistry (i.e., pH, short-chain PFAS formation, fluoride concentration) and V(V)-C nanosheet physicochemical evolution (i.e., morphology, surface vanadium valence state) were performed to elucidate PFOS removal and defluorination mechanisms.

Materials and methods

V(V)-C nanosheet preparation

A list of chemicals and materials used in this study is provided in the Supporting Information (SI). The V_2C nanosheet was synthesized from purchased V_2AlC MAX phase powder following methods reported in the literature.³⁶ Briefly, 10 mL of hydrofluoric acid (HF) and a magnetic stir bar were added to a 50-mL

polypropylene flat-bottom bottle. Approximately 1 g of the V_2AlC MAX phase powder was slowly added and mixed into 30% HF acid aqueous solution in the bottle, then the bottle was capped loosely and sealed with parafilm. The HF and V_2AlC solution were stirred at 150 rpm every 12 hrs over 7 days to etch the Al in the MAX phase. After the 7-day mixing period, the HF-etched V_2C powder mixture solution was washed with ultrapure water (resistivity 18.2 $\text{M}\Omega\text{-cm}$) until the wash pH was 6.0. The washed sample was freeze-dried under vacuum overnight³⁷ for further analysis. The interlayer spacing between the etched, freeze-dried V_2C was increased during intercalation by mixing with 30 mg/mL dimethyl sulfoxide (DMSO). Delamination was achieved by sonicating the intercalated powder that separated from DMSO after intercalation under atmospheric conditions, then the collected supernatant was sonicated, which led to the formation of V(V)-C nanosheet solution. The V(V)-C solution was purified using Spectra/Por (VWR International, LLC, PA) cellulose acetate membrane dialysis tubing (300–500 Da) for 7 days to remove residual fluoride from the HF etching process.

Material synthesis characterization

Scanning electron microscopy (SEM, JEOL 7000F, 10 kV accelerating voltage, Tokyo, Japan) was used to visualize the morphology of the V_2AlC MAX phase, etched V_2C , and as-prepared V(V)-C nanosheets. Mineral phase identification of the commercial MAX phase, etched, and delaminated phases were examined using X-ray diffraction (XRD, Bruker D8 ADVANCE Eco, MA).

The vanadium oxidation state on the V(V)-C nanosheets before and after the reaction with H_2O_2 was identified using XPS (Surface Science Instruments S-Probe spectrometer, OR). To examine changes in the vanadium oxidation state due to the reaction with H_2O_2 , a V(V)-C and H_2O_2 mixture was reacted for 2 hrs and then measured with XPS. XPS analysis was also performed to identify new bond formation and vanadium oxidation state changes following PFOS transformation by V(V)-C nanosheets by adding 300.5 $\mu\text{g/L}$ PFOS.

The V(V)-C nanosheet zeta potential profile was obtained at different initial pH values to determine their surface charge. Triplicates of V(V)-C nanosheet solution were prepared at initial pH values of 2, 4, 6, 8, and 10. The resulting surface charge was measured using a Zetasizer (Malvern 1011155 Zetasizer Nanoseries, MA). To better understand the mechanisms occurring during PFOS transformation, the pH of solutions containing combinations of 0.15 mg/mL V(V)-C nanosheets, 14.7 mM H_2O_2 and 50 $\mu\text{g/L}$ PFOS **V(V)-C+ H_2O_2** , and the control solutions (i.e., without PFOS, **blank V(V)-C+ H_2O_2**) were measured as a function of time.

To detect the formation of radical species from V(V)-C nanosheets and V(V)-C nanosheet reactions with H_2O_2 in solution, EPR (electron paramagnetic resonance, Bruker EMX, MA) spectra were obtained at 9–10 GHz. A 20 mM 5,5-Dimethyl 1-pyrroline N-oxide (DMPO) capture was used to trap generated hydroxyl radicals and solvated electrons, and 20 mM 2,2,6,6-tetramethyl-4-piperidone (TEMP) was added to form adducts and capture singlet oxygen reactive species for EPR detection. The reaction systems contained 0.15 mg/mL V(V)-C nanosheets and/or 14.7 mM H_2O_2 in ultrapure water. Capture agents were added after mixing the reaction

components for less than 1 min. More detailed information on the characterization and synthesis of V(V)-C is described in **Section SI**.

PFOS degradation and defluorination kinetics experiments

Batch PFOS transformation kinetics studies were performed using four reaction systems: **blank** (50 $\mu\text{g/L}$ PFOS only), **H₂O₂** (50 $\mu\text{g/L}$ PFOS and 14.7 mM H₂O₂), **V(V)-C** (50 $\mu\text{g/L}$ PFOS and 0.15 mg/mL V(V)-C), and **V(V)-C+H₂O₂** (50 $\mu\text{g/L}$ PFOS, 0.15 mg/mL V(V)-C and 14.7 mM H₂O₂). A 6.2 mL reaction solution was prepared in 15 mL polypropylene centrifuge tube for each system and all systems were prepared in triplicate in sacrificial samples. Tert-butyl alcohol (final concentration: 158 mM) was added upon sampling to scavenge hydroxyl radicals formed from the degradation of H₂O₂ in water.³⁸ Then the solutions were filtered using a 0.20 μm cellulose acetate syringe filter (VWR International, LLC, PA). Preliminary tests with different filter materials indicated that filtration using a cellulose acetate syringe filter resulted in the least amount of PFOS loss (i.e., less than 13% of PFOS lost at 50 $\mu\text{g/L}$ initial concentration) compared with nylon syringe filters (99–100% PFOS loss) and PES syringe filters (89% PFOS loss). The first 250 μL of the filtrate was discarded during filtration to decrease the amount of PFAS loss to the cellulose acetate filters. The samples were then prepared for PFAS detection and quantification using liquid chromatography-tandem mass spectrometry (LC-MS/MS) analysis using the method described in **Tables S5, S5a, and S5b**. Detailed descriptions of PFOS quantification are provided in **Tables S2, S3, and S4** and **Section SII**).

The extent of defluorination within different reaction systems was quantified using ion chromatography (IC, Dionex DX-120, Fisher Scientific, MA). Defluorination calculation details are provided in Table S6. The ion chromatography limit of detection for fluoride is 18.99 $\mu\text{g/L}$ (1 μM). To determine the F⁻ concentration more accurately, the samples were filtered through a 0.02 μm aluminum-based syringe filter (Aluminum base, Whatman Inc., Maidstone, United Kingdom) at the end of the reaction period to increase the separation of V(V)-C nanosheet compared to the 0.20 μm syringe filters used previously for LC-MS/MS analysis. Experimental procedures regarding the use of 0.02 μm syringe filters are described in **Section SI**.

Results and discussion

As-prepared V(V)-C nanosheet structure characterization

The molecular and structural evolution of the V₂C nanosheet material during synthesis is depicted in **Fig. 1** and captured using scanning electron microscopy. The resulting layered V₂C MXene structure (**Fig. 1a2, b2**) produced from HF etching of the V₂AlC MAX phase powder (**Fig. 1a1, b1**) indicates 10–100 nanometers of interlayer space was created following etching, generating single layer nanosheets with a thickness around 250 nm (**Fig. S1b**). The DMSO intercalation process was used to weaken van der Waals attractive forces and hydrogen bonding interactions among V₂C MXene layers and increase layer spacing before sonication to produce delaminated V₂C nanosheets suspended in solution. V₂C MXene nanosheets can be easily hydrolyzed into vanadium oxide

(V₂O₅) in aerated water,³⁹ forming a hydrolyzed vanadium carbon composite heterostructure (i.e., V(V)-C). The structural identity of the materials was determined using XRD (**Fig. 1c**) and UV (**Fig. S1a**). The presence of small peaks in the 200 nm range of a UV spectral scan (**Fig. S1a**) indicates that while some V₂C nanosheets remain, the majority of the nanosheets exist as oxidized vanadium(V) phases closely associated with graphitic carbon. The V₂AlC spectra show two characteristic MAX phase peaks of (006) at a 2 θ of 41.3° signifying Al atomic layers, and (002) at 13.5° which corresponds to MAX phase interlayer distances.²⁴ After etching, the largest (006) peak is suppressed, and the (002) peak is broadened and downshifted significantly. The shift is due to interlayer spacing expansion caused by replacing Al atomic layers with functional groups (=O, -OH, and -F), and intercalation of water and DMSO molecules during the etching process.²⁴ The spectra of the delaminated nanosheet suspension shows the total disappearance of the (002) at 11° peak, suggesting undetectable amounts of multi-layered MXene structures in the supernatant solution. After delamination and hydrolysis, the (002) V₂C MXene peak shifted to 27.2° which was identified as graphitic carbon⁴⁰ and suggests that carbon nanosheets are the dominant phase in solution. Hence, the as-prepared V₂C solution is composed of trace amounts of V₂C nanosheets (**Fig. S1a**) and oxidized vanadium(V) phases within single-layer carbon (i.e., “V(V)-C”, **Fig. 1a3, b3, Fig. 1c, and Fig. S2**) due to the sonication, purification, and storage processes which exposed V₂C nanosheets to oxygen which hydrolyzed the nanomaterials in water.

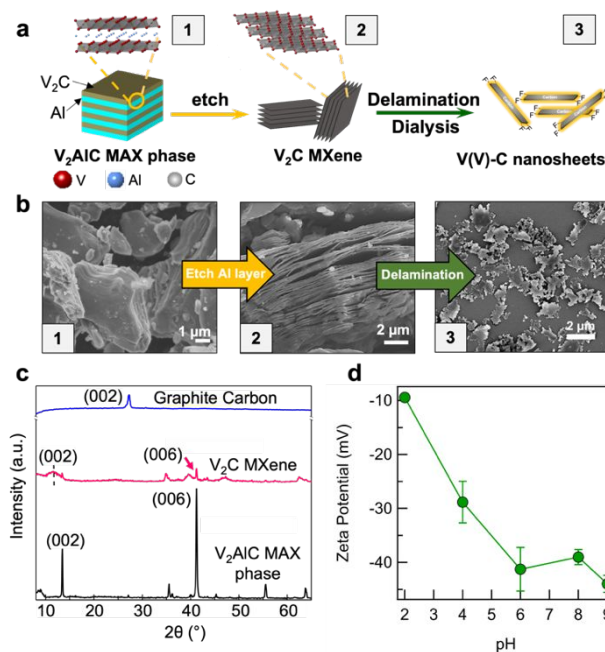


Figure 1 (a) Schematic of V(V)-C nanosheet preparation and (b) SEM images of (1) the V₂AlC MAX phase material, and (2) resulting V₂C layers generated from selectively etching the Al layer. The spacing between the V₂C layers increased during intercalation by DMSO addition which facilitates (3) delamination of V₂C to form V(V)-C nanosheets upon ultrasonication. (c) XRD spectra for V₂AlC (bottom), etched V₂C MXene (middle), and V(V)-C nanosheets (top). (d) Surface charge profile for 0.15 mg/mL V(V)-C nanosheets in solution as a function of pH indicating negative surface charge over a broad pH range.

To gain additional insight into the chemical behavior of V(V)-C, the V(V)-C surface charge was determined as a function of solution

pH to better understand their aqueous stability and interactions with negatively charged PFOS (Fig. 1d). V(V)-C suspensions in ultrapure water had an overall negative surface charge with values ranging from -9.4 ± 0.69 mV (pH 2) to -44.0 ± 1.58 mV (pH 10). The negative surface charge is assumed to originate from the abundance of oxygenated and fluorinated moieties terminating functional groups present on V(V)-C nanosheets. This finding is consistent with observed negative surface charges on graphitic materials (e.g., activated carbon and graphene nanosheets) which have been widely used and/or exploited for PFAS uptake.^{41,42}

Rapid and near-complete PFOS defluorination by V(V)-C+H₂O₂ system

Batch kinetics experiments were performed to assess transformation and degradation rates of PFOS by the as-prepared V(V)-C (Fig. 2a). Only 2% PFOS removal was detected in the H₂O₂ control system within the reaction period, which was attributed to statistical and human error in sample preparation and analysis, and not to any PFOS transformation.⁴³ The optimal reaction mixture was the V(V)-C+H₂O₂ system which resulted in rapid removal: 96% PFOS removal after 4 hrs was observed with 84% removal occurring within the first 30 min. Though the V(V)-C system also exhibited rapid initial PFOS removal within the first 5 min of reaction, though the final PFOS removal reached a lower PFOS removal after 4 hrs (62%). The performance of the as-prepared V(V)-C for PFAS removal remained stable even after being exposed to air for over a year, as indicated in Table S10.

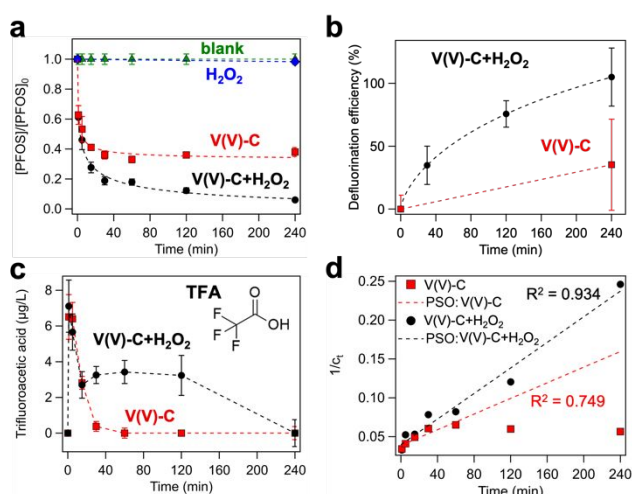


Figure 2 (a) Normalized PFOS removal kinetics results determined using LC-MS/MS. 50 µg/L PFOS was treated with combinations of 0.15 mg/mL V(V)-C nanosheets and/or 14.7 mM H₂O₂ in ultrapure water. The Blank profile contained only 50 µg/L PFOS. (b) PFOS defluorination efficiency for the V(V)-C+H₂O₂ and V(V)-C reaction systems as a function of time. Trifluoroacetic acid (TFA) concentrations were detected in the samples corresponding to (c) as a function of time. (d) Linearized pseudo-second-order kinetics fitting and correlation coefficients (R²) for the V(V)-C and V(V)-C+H₂O₂ reaction systems.

Analysis of aqueous F⁻ concentrations reveal that PFOS defluorination occurred in the V(V)-C+H₂O₂ reaction system; however, no significant defluorination was observed in the V(V)-C system (Fig. 2b). Residual F⁻ was present in V(V)-C samples even after dialysis purification processes. Therefore, to account for the F⁻ response from V(V)-C, a 0.15 mg/mL V(V)-C only control was

measured with IC and the corresponding F⁻ concentration was subtracted from the final F⁻ concentration of the reaction systems. The IC data indicates near-complete defluorination (i.e., $105 \pm 23\%$) was achieved in the V(V)-C+H₂O₂ system within 4 hrs. These results are extremely promising compared to defluorination efficiencies and rates of other reported homogeneous and heterogeneous PFAS degradation approaches (Table 1). While the initial conditions and methods of PFAS degradation provided in Table 1 differ from the conditions explored in this study, our findings indicate that the V(V)-C+H₂O₂ approach is among the fastest with the highest defluorination efficiency.

Table 1 Comparison of reported PFAS degradation methods, reaction times, and defluorination efficiencies

methods	initial PFAS concentration	reaction duration ^d	defluorination ion efficiency	byproduct formation
UV ^a direct photolysis $\lambda = 220-460$ nm ⁴⁴	29.6 µmol PFOA	72 hours	89.5% degraded	F ⁻ and CO ₂ , C1-C6 short chain fluorinated carboxylic acid
H ₂ O ₂ and iron (III) ⁴³	100 µg/L PFOA	2.5 hours	89% removed and about 89% defluorinated ion	F ⁻ and no detectable products
laccase-catalyzed reaction ⁴⁵	414 µg/L PFOA	157 days	50% removed and 28.2% defluorinated ion	F ⁻ and no detectable products
heterogeneously catalyzed ozonation	160 µg/L	3 hours	C12-C17: 64%	
iron-oxide based catalyst ²⁰	C4-C7 PFAS		C7-C11: >98%	not mentioned
HDTMA-coated clay/IAA/UV ^b combined system $\lambda = 254$ nm ¹	10 mg/L PFOA	10 hours	100% removed and 90% defluorinated ion	C1-C6 fluorinated carboxylic acid
V(V)-C+H ₂ O ₂ system (this study)	50 µg/L PFOS	4 hours	96% removed and near 100% defluorinated ion	TFA and F ⁻

Notes: a) UV: ultraviolet; b) IAA: 3-indole-acetic-acid, HDTMA: hexadecyltrimethylammonium bromide; c) includes the corresponding reaction rate constant (k) and the half-life time (t_{1/2}) of PFAS(s); d) The length of the time required for the maxi it took to reach maximum removal efficiency detected with LC-MS/MS.

Target LC-MS/MS analysis indicated the formation of trifluoroacetic acid (TFA), a short-chain PFAS, in the V(V)-C and V(V)-C+H₂O₂ reaction systems (Fig. 2c) during the reaction. Information

regarding accurate quantification of TFA in samples containing tert-butyl alcohol is provided in **Section SV**. Previous studies investigating PFOS degradation report the formation of short-chain perfluorocarboxylic acids (e.g., TFA) via cleavage of centermost C–C bonds or C–F bonds during incomplete PFOS mineralization;¹ therefore, generation of TFA in these systems further signifies degradation occurred. The TFA generated in the **V(V)-C** system was quickly formed in the first minute (up to 6.5 $\mu\text{g/L}$ TFA), and then continued to decrease until TFA was undetectable (after 1 hr). Based on this observation, we hypothesize that PFOS degradation on the V(V)-C nanosheet surface is limited in the absence of H_2O_2 . For the **V(V)-C+H₂O₂** reaction system, 7.1 $\mu\text{g/L}$ TFA was detected within the first minute of the reaction, which suggests rapid PFOS degradation. Initially, the generation of TFA is faster than the defluorination of TFA, leading to an increase in TFA concentration. However, as less PFOS remains in solution, the generation of TFA and defluorination reach a dynamic equilibrium. When all of the PFOS has degraded, and the TFA formation stops and its concentration begins to decrease, the initial PFOS is fully defluorinated (**Fig. 2c**). For example, the TFA concentration in the **V(V)-C+H₂O₂** reaction system decreased to 2.5 $\mu\text{g/L}$ after 15 min, which mirrors the observed accelerated PFOS removal within the first 15 min of the reaction (**Fig. 2a**). After 30 min, the TFA concentration achieved a pseudo steady state value for 1.5 hrs until no TFA was detected at the end of the reaction period. No other short-chain (e.g., C7–C3)¹ PFAS were detected in either reaction system. Compared with other reported systems¹, the lack of other detectable short-chain PFAAs could be due to several possibilities. (1) The **V(V)-C** and **V(V)-C+H₂O₂** systems may exhibit highly efficient PFAS defluorination which bypasses the formation of other intermediate PFAAs. (2) Other short-chain PFAAs were rapidly formed, remained adsorbed to the V(V)-C nanosheet surface following initial PFOS adsorption, then degraded immediately to TFA. For example, F⁻ can also adsorb to V(V)-C nanosheets according to a batch isotherm experiment (described in **Fig. S6**).

Kinetic modeling of PFOS degradation in the **V(V)-C+H₂O₂** and **V(V)-C** reaction systems further corroborated the PFOS removal and degradation data (**Fig. 2d**). Kinetics modeling information is provided in **Section SIII**. Both systems were evaluated with pseudo-first-order and pseudo-second-order rate models.⁴⁶ In contrast to previously reported systems,^{17,47,48} the **V(V)-C+H₂O₂** system was best described by pseudo-second-order kinetics which revealed that PFOS removal was primarily controlled by defluorination kinetics, while PFOS removal in the **V(V)-C** system is only minimally impacted by defluorination kinetics.⁴⁶ For example, the **V(V)-C** system was only well described by pseudo-second-order reaction kinetics for the first 15 to 30 min, after which the observed PFOS degradation rate diverged significantly from the predicted rate (**Fig. 2d** and **Fig. S7**). PFOS degradation in the **V(V)-C+H₂O₂** system was observed at a rate of $k = 0.0008 \text{ L}/\mu\text{g}\cdot\text{min}$ with a corresponding half-life $\tau_{1/2} = 48 \text{ min}$, which is much faster than the destruction rates reported in other studies (**Table 1**). The kinetics fit divergence is also evident in the poor pseudo-second-order fit for the **V(V)-C** system ($R^2 = 0.749$) compared to the **V(V)-C+H₂O₂** system fit ($R^2 = 0.934$). An aqueous PFOS equilibrium concentration was achieved after 60 min of

reaction in the **V(V)-C** system (**Fig. 2a**), which is the time at which the pseudo-second-order degradation fit begins to diverge. Therefore, we postulate that the physical adsorption of PFOS onto the V(V)-C nanosheet surface is the primary PFOS removal mechanism during the initial stage of the **V(V)-C** system kinetics. Two removal processes appear to be occurring at the same time in the **V(V)-C + H₂O₂** system based on interpretations of the pseudo-second-order fit: (1) a fast PFOS adsorption period within the first 60 min (similar to the **V(V)-C** system); and, (2) slower reaction kinetics after 60 min which may be attributed to PFOS defluorination kinetics.

To further characterize PFOS degradation in the **V(V)-C** and **V(V)-C + H₂O₂** systems, IC was used to detect fluoride released as a function of time (**Fig. 2d**). Residual F⁻ was present in V(V)-C samples even after dialysis purification of the nanosheet suspension. The PFOS defluorination efficiency was determined by subtracting the F⁻ concentration in control samples (0.15 mg/mL V(V)-C). No additional F⁻ release was detected in the V(V)-C solution following a 4-hour reaction with 14.7 mM H_2O_2 (**Table S9**). Therefore, to account for the F⁻ response from V(V)-C, the **blank V(V)-C** system (i.e., 0.15 mg/mL V(V)-C only) was measured as a blank control sample. Furthermore, the **V(V)-C** reaction system was also measured as a control sample to eliminate any interference from PFOS peaks in the IC spectra. The IC data indicates near-complete defluorination (i.e., $105 \pm 23\%$) was achieved in the **V(V)-C + H₂O₂** system within 4 hrs. These results are extremely promising compared to other reported homogeneous and heterogeneous PFAS degradation approaches (**Table 1**).

In addition to the rapid, near complete defluorination observed in our **V(V)-C + H₂O₂** system, only TFA (C2) byproducts were detected compared to C7–C3 perfluoroalkyl acid (PFAA) byproducts formed and detected in other studies. For example, Tian et al. identified the formation of C6–C2 perfluorocarboxylic acids in addition to TFA after 24-hr reductive PFOA and PFOS defluorination on organoclays.¹ The lack of other detectable short-chain PFAAs could be due to several possibilities. (1) The **V(V)-C** and **V(V)-C + H₂O₂** systems may exhibit highly efficient PFAS defluorination which bypasses the formation of other intermediate PFAAs. (2) Other short-chain PFAAs were rapidly formed, remained adsorbed to the V(V)-C nanosheet surface following initial PFOS adsorption, then degraded immediately to TFA. The presence of –F termination on V(V)-C nanosheet surfaces may enhance the adsorption of PFOS C–F via F–F interactions.⁴⁹ PFOS adsorption to V(V)-C nanosheets may facilitate transformation by shortening the distance between PFOS and reactive species generated near the V(V)-C nanosheet catalytic reaction center,²⁴ which is advantageous compared to bulk-phase PFAS degradation processes. In contrast, the **V(V)-C** reaction system yielded negligible fluoride release; yet, TFA byproduct formation was identified in **Fig. 2c**. These data suggest that V(V)-C nanosheets can facilitate PFOS degradation in the absence of H_2O_2 , but defluorination may require additional chemical or energy inputs.

Enhanced solvated electron formation in the **V(V)-C+H₂O₂** system

The observed degradation and defluorination by the V(V)-C containing reaction systems must be due to electron transfer within or on V(V)-C capable of cleaving PFOS C–F and C–C bonds. Based on the study by Li *et al.*, the reaction between a V_2O_5 artificial enzyme

can shuttle electrons by reacting with H_2O_2 . They hypothesized that vanadium centers within V_2O_5 possess depressed d-orbital electron density, and the V-d orbitals readily form sigma bonds with H_2O_2 oxygen-p orbitals for diminished catalytic activity.⁵⁰ They further posit that coordination of the V_2O_5 with a Zn^{2+} electron donor to form Zn–O–V bonds was found to stabilize electron transfer from Zn to the vanadium center, inhibit the sigma bond formation between the vanadium d-orbital and the H_2O_2 oxygen p-orbitals, and enhance the formation of reactive species in solution. In our as-prepared V(V)-C material, we hypothesize that the carbon bonded to the V(V) phases (generated from the hydrolysis of V_2C) serves as the electron donor to stabilize reactions with H_2O_2 ^{51,5} in the same way that Zn is stabilizing electron transfer in the Li et al. study. When adding H_2O_2 , the electron transfer from the carbon to V_2O_5 phases could be catalyzed. Given the fact that our V(V)-C+ H_2O_2 reaction system has a two-electron transfer as the V(V) phases are reduced to V(III) phases, the excess electrons transferred could be surrounded by water to form solvated electrons. Andris et al. demonstrated that vanadium oxide phases can be reduced during hydrothermal treatment in the presence of graphitic carbon via the generation of a $\delta\text{-C}_x\text{V}_2\text{O}_5\cdot n\text{H}_2\text{O}$ heterostructure.⁵¹ V(V)-C solution. Therefore, we hypothesize that electron transfer from carbon to vanadium oxides can occur upon chemical (or thermal) activation. To validate this assumption, the pre- and post- H_2O_2 reaction vanadium oxidation state was determined by XPS (Fig. 3). The initial vanadium oxidation state was confirmed to be mostly vanadium(V) (e.g., V_2O_5) phases which are then reduced to vanadium (III) (e.g., V_2O_3) phases after reacting with H_2O_2 (Fig. 3a, b and Table 2, Fig. S7). The C1s XPS spectra of V(V)-C before and after reacting with H_2O_2 indicates that vanadium reduction is accompanied by oxidation of carbon in the material (Fig. 3c, d and Table 2). The ability of V(V)-C to promote rapid electron transfer following a stimulus (e.g., applied potential) has been well documented.^{24,52} Evidence of oxidation state changes within the V(V)-C suggests that electron shuttling may occur at/near the nanosheet reaction center which would then influence nearby adsorbed PFOS.

Table 2 Information regarding peak identification for the different reaction systems in Fig. 3.

	peak ID	binding energy (eV)	abundance (%)	reference ID	Ref.
blank V(V)-C	V 2p _{3/2}	516.5	2.8	516.4 eV (V ⁵⁺)	[53]
	V 2p _{3/2}	517.7	18.1	517.7 eV (V ⁵⁺)	[54]
	V 2p _{1/2}	524.7	11.8	524.5 eV (V ⁵⁺)	[55]
	V-O1s	530.6	22.3	530.5 eV (V ₂ O ₅)	[55]
	C-C	285.0	58.7	ubiquitous C	[56]
	C-O	283.8	19.6	oxidized C	[57]
blank V(V)-C +H ₂ O ₂	V 2p _{3/2}	515.9	16.9	515.7 eV (V ³⁺)	[58]
	V 2p _{1/2}	522.8	10.0	523.0 eV (V ³⁺)	[58]
	V-O1s	530.5	20.4	530.5 eV (V ₂ O ₅)	[55]
	C-C	285.0	10.1	ubiquitous C	[56]
	C-O	283.6	86.7	oxidized C	[57]

Reactive species formation detected using EPR suggests singlet oxygen ($^1\text{O}_2$, Fig. S4a), hydroxyl radical (HO^\bullet , Fig. S5), and solvated electron (Fig. S5) formation in V(V)-C+ H_2O_2 systems. The formation of HO^\bullet is expected due to H_2O_2 decomposition,^{50,59} no obvious superoxide radicals was observed in this system.⁶⁰ However, the $^1\text{O}_2$ formation is an interesting observation. We hypothesize that $^1\text{O}_2$ generation could occur via the biomimetic vanadium(V) haloperoxidase mechanism (Fig. S4c reaction pathway B) which has been reported for V_2C MXenes in other studies.⁶¹ It is well-known that HO^\bullet and $^1\text{O}_2$ are extremely inefficient in cleavage of C–F bonds due to the lack of extractable hydrogen atoms within the PFOS structure.⁶² However, the presence of solvated electron can initiate the defluorination of PFOS by cleaving C–F and then form C–H, and then further degradation can be facilitated by HO^\bullet , $^1\text{O}_2$ and additional solvated electrons. Hence, solvated electron formation in the V(V)-C+ H_2O_2 reaction system (Fig. S5) is most likely the reactive species responsible for initiating PFOS degradation. The weak solvated electron signal implies that the highly reducing species are formed within or strongly associated with the V(V)-C nanosheets, and not in the bulk solution. We hypothesize that solvated electron generation in the V(V)-C and V(V)-C+ H_2O_2 systems were responsible for TFA formation and subsequent PFOS defluorination. To confirm this hypothesis, 20 mM DMPO was added as a solvated electron capture agent in these reaction systems to form detectable DMPO–H adducts during EPR measurement.⁴⁷ To further clarify the role of solvated electrons in PFOS defluorination, additional tests were conducted to identify PFOS transformation and F⁻ release upon quenching solvated electron formation at different initial PFOS concentrations. A batch test was conducted by adding 10 mM

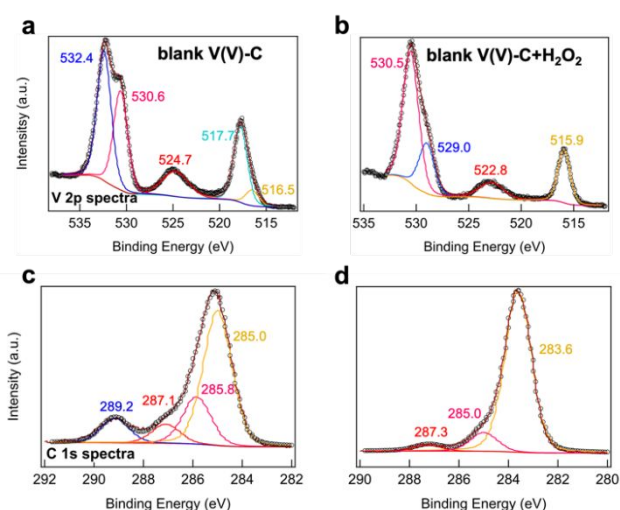


Figure 3 Fitted XPS V 2p spectra of (a) blank V(V)-C (0.15 mg/mL V(V)- V_2C) and (b) blank V(V)-C+ H_2O_2 (0.15 mg/mL V(V)- V_2C , excess H_2O_2) reaction systems reacted for 2 hrs. The corresponding C 1s spectra for these systems are provided in (c) and (d), respectively.

sodium nitrate (NaNO_3)—a known solvated electron scavenger¹⁵ to 300.5 $\mu\text{g/L}$ PFOS and V(V)-C nanosheets to assess PFOS defluorination and validate our hypothesis that solvated electron generation is primarily responsible for PFOS transformation. This mixture was reacted for 4 hrs and then measured using IC (Fig. 4a) and XPS (Fig. 4c, d, and Table 3). When NaNO_3 was added, the calculated PFOS defluorination efficiency was only $3.33 \pm 4.31\%$ compared to $41.31 \pm 16.47\%$ defluorination efficiency when no NaNO_3 was added (Fig. 4a). This result confirmed that PFOS transformation was driven by solvated electron formation in the V(V)-C+ H_2O_2 system. The reason for the lower defluorination efficiency in the sample without NaNO_3 , compared to the results shown in Fig. 2b, is that a higher initial PFOS concentration was used in this test to promote PFOS transformation.

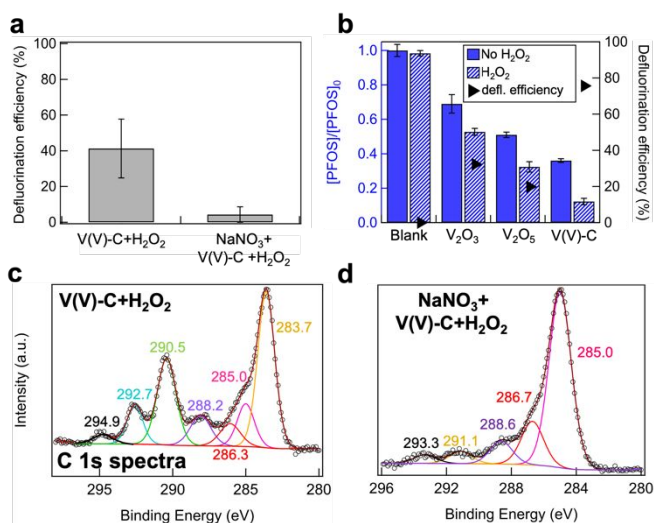


Figure 4 (a) Defluorination of V(V)-C+ H_2O_2 (300.5 $\mu\text{g/L}$ PFOS, 0.15 mg/mL V(V)-C nanosheets, 14.7 mM H_2O_2) in the presence (NaNO_3 +V(V)-C+ H_2O_2) and absence of 10 mM NaNO_3 to quench solvent electron generation. (b) PFOS removal (left axis) and the corresponding defluorination efficiency (right axis) were measured by ion chromatography comparing different vanadium-containing reaction systems for PFOS defluorination by reacting 50 $\mu\text{g/L}$ PFOS with and without 14.7 mM H_2O_2 for 2 hrs in ultrapure water. The reaction systems include Blank (no vanadium species added); V_2O_3 (a saturated solution, pH 3.8, of commercial V_2O_3); V_2O_5 (a saturated solution, pH 3.8, of commercial V_2O_5); and, V(V)-C as reported in Fig. 2d. (c) Fitted XPS C 1s spectra of the V(V)-C+ H_2O_2 and (d) NaNO_3 +V(V)-C+ H_2O_2 reaction systems reacted for 2 hours. In both reaction systems, 100 $\mu\text{g/L}$ PFOS, 0.15 mg/mL V(V)-C nanosheets and 14.7 mM H_2O_2 were added. The NaNO_3 +V(V)-C+ H_2O_2 system contained 10 mM NaNO_3 added at the start of the reaction.

Table 3 Information regarding peak identification for the different reaction systems in Fig. 4 c, d

	peak ID	binding energy (eV)	abundance (%)	reference ID
V(V)-C+ H_2O_2	CHF-CF ₂	290.5	22.9	290.8 eV ⁶³
	CF ₂	292.7	7.7	292 eV ⁶⁴
NaNO ₃ +V(V)-C+ H_2O_2	CF ₂ -CHF	291.1	4.7	290.8 eV ⁶³

At an initial PFOS concentration of 100 $\mu\text{g/L}$, XPS C1s spectra revealed the formation of CHF-CF₂ bonds in the V(V)-C+ H_2O_2 system at 23% abundance after 2 hrs of reaction. Adding 10 mM NaNO_3 to

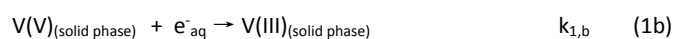
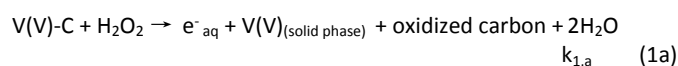
this reaction system decreased the abundance of CHF-CF₂ bonds to only 4.7% (Fig. 4 c, d and Table 3). These data strongly indicate that solvated electrons generated in the V(V)-C+ H_2O_2 systems are the primary reactive species responsible for PFOS destruction. Additional information about this test is provided in Section SIV.

V(V)-C facilitated solvated electron formation and H_2O_2 -catalyzed PFOS defluorination on V(V)-C nanosheet surfaces

There are three primary observations for this study: (1) rapid, efficient PFOS removal by as-prepared V(V)-C nanosheets; (2) formation of reactive (oxygen) species such as hydroxyl radicals, singlet oxygen in solution and solvated electrons near V(V)-C (particularly in H_2O_2 -containing reaction systems); and, (3) near-complete PFOS defluorination on V(V)-C nanosheets catalyzed by the addition of H_2O_2 .

Solvated electrons are hypothesized to form within or closely associated with V(V)-C surfaces near adsorbed PFOS to initiate defluorination. The large V(V)-C nanosheet surface serves as a reaction center where the solvated electrons can then easily transfer from the V(V)-C to PFOS and initiate degradation and defluorination at enhanced rates and efficiencies compared to other reported advanced oxidation/reduction reaction systems (Table 1).^{1,65} The rapid electron charge transfer kinetics between the electronegative moieties of adsorbed PFOS, vanadium(V) and graphite carbon generated from V_2C^{51} (i.e., formation of C-O and C-OH observed in V(V)-C+ H_2O_2 XPS spectra, Fig. S2 and Table S7) combined with the reversible nature of vanadium oxidation states within V(V)-C could provide enough energy to form solvated electrons near co-located PFOS. In our study, the solvated electron (e^-_{aq}) formation is catalyzed upon the addition of H_2O_2 which corresponds to vanadium oxide reduction (from V(V) to V(III)) and carbide oxidation (increase in C-O abundance and decrease in C-C abundance Table 2).

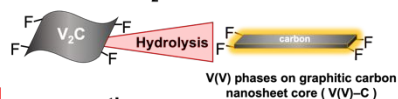
As stated previously, the conductivity of the carbide layer within MXenes (including with our as-prepared V(V)-C nanosheets, Fig. S8) can enable the transport of electrons and produce radical species (e.g., during polymerization). For example, a study by Mashtalir et al.³⁰ investigating photocatalytic degradation of methylene blue by Ti(II)-phase Ti_3C_2 MXenes observe a two-electron phase change (from Ti(II) to Ti(IV)- TiO_2) within MXenes following adsorption of methylene blue (dark conditions) over a period of one week. Dissolved oxygen present in the reaction solution was hypothesized to consume Ti and C to form TiO_2 phases and carbon dioxide. We propose similar reaction mechanisms occurring within the V(V)-C+ H_2O_2 reaction systems:



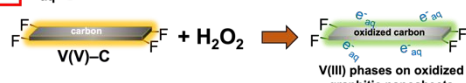
The rate of solvated electron generation ($k_{1,a}$) is assumed to be much greater than the solvated electron consumption rate ($k_{1,b}$) in the V(V)-C+ H_2O_2 system.

Upon addition and adsorption of PFOS to the V(V)-C nanosheet surface, we propose the following two mechanisms may occur to enhance degradation and defluorination in the presence of H_2O_2 .

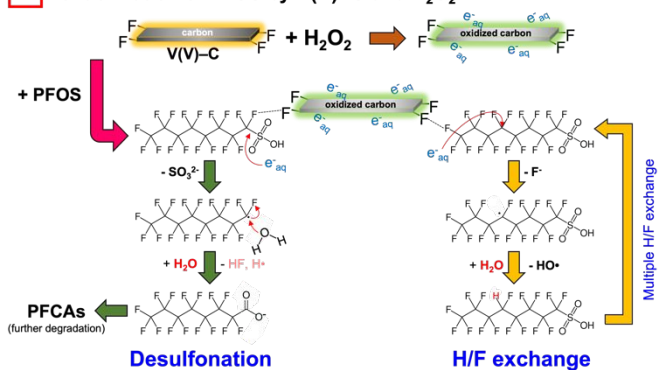
1 Oxidation of V₂C nanosheet



2 e_{aq}⁻ generation



3 Defluorination of PFOS by V(V)-C and H₂O₂



Scheme. The proposed interactions of PFOS, V(V)-V₂C, and H₂O₂ in our study facilitate PFOS degradation and defluorination. **(1)** The formation of the initial V(V)-C nanosheet vanadium oxidation state contains an oxidized vanadium phase on graphitic carbon nanosheets resulting from the synthesis of V₂C nanomaterials. **(2)** The addition of H₂O₂ catalyses the V(V) to V(III) phases and formation of solvated electrons (e_{aq}⁻). **(3)** Two PFOS defluorination mechanisms could occur in our reaction system. PFOS fluorine atoms adsorb to fluorine atoms along the V(V)-C nanosheet edges. **Desulfonation:** Solvated electrons attach at the sulfonic head group to form a short-lived radical. Adding H₂O and abstraction of H and F atoms facilitates the formation of perfluorooctanoic acid, which, upon subsequent attack by solvated electrons, ¹O₂ and HO[•] radicals, forms short chain perfluorocarboxylic acids (PFCAs). **H/F exchange:** Solvated electrons attack the weakest, centremost C–F bond to form a PFOS radical. Adding H₂O replaces the F atom with a H (i.e., –CHF bonds), and subsequent attack by solvated electrons will propagate F abstraction to form short-chain PFAS intermediates and compounds more readily degraded by ¹O₂ and HO[•].

The first hypothesis is that PFOS fluorine form a complex with the high valent vanadium oxide phases (i.e., V₂O₅) wherein fluorine atoms are abstracted and replaced with hydrogen atoms. Vanadium oxide–fluorine complexes have been established in the literature,^{66,67} and the formation of –CHF bonds may be evidenced by the XPS spectra could be due to fluorine abstraction (**Fig. 4c,d** and **Table 3**).

Our second hypothesis is that during initial defluorination, solvated electrons and reactive oxygen species (hydroxyl radicals and singlet oxygen) are activated by electron-deficient vanadium transition-metal coordination processes within the vanadium(V) nanomaterial.⁶⁸ Literature purporting degradation pathways for PFAS suggests that degradation activation by single electron transfer is the rate-limiting step⁶⁹ which is followed by rapid, subsequent defluorination and byproduct formation. The XPS analysis (**Fig. 3**, and **Table 2**) indicates that a two-electron transfer occurs within the V(V)-C nanosheet as the vanadium(V) phases are reduced to vanadium(III) phases which could help overcome the slow electron transfer activation. In electrochemical, catalytic and heterogeneous advanced oxidation processes, vanadium(V) oxidation states have demonstrated rapid and reversible charge transfer kinetics and reactivity.^{24,70,71} Therefore, vanadium(V) oxidation states within the

V(V)-C nanosheet may exhibit high electron shuttling capacity⁷² and contribute to the formation of reactive (oxygen) species. The **Scheme** outlines hypothesized PFOS defluorination processes in which solvated electron generation and two-electron transfer occurs (**Scheme 2**) can facilitate and propagate defluorination in the V(V)-C+H₂O₂ systems (**Scheme 3**). The desulfonation and H/F exchange processes proposed in the literature^{73,74} for bulk-phase defluorination of PFOS were adapted for the V(V)-C+H₂O₂ reaction system. **Scheme 3 Desulfonation:** Solvated electrons cleave the PFOS C–S bonds which produces a short lived [•]C_nF_{2n+1} radical. Hydroxylation of the radical (addition of –OH) followed by sequential eliminations of H⁺ and F⁻ moieties to form perfluorocarboxylic acids. **Scheme 3 H/F exchange:** Solvated electrons can cleave centremost C–F bonds within PFOS which have the lowest bond dissociation energy to produce radicals. Addition of H₂O molecules forms –CHF bonds which are observed in our study. Multiple exchanges of F⁻ with H atoms can promote additional attack by accompanying reactive oxygen species. For instance, HO[•] and ¹O₂ species generated in the same reaction process (**Fig. S3** and **S5**) can react with newly-formed –CHF bonds produced from initial PFOS defluorination to increase the PFOS degradation rates and efficiencies (**Table 3**). Furthermore, nitrate scavenging addition of solvated electrons resulted in lower –CHF peak area (**Fig. 4c, d** and **Table 3**). This evidence further suggests that solvated electrons are critical for PFOS defluorination in the V(V)-C+H₂O₂ reaction system.

To further understand the roles of V(V)-C vanadium oxidation states, vanadium ions, and heterogeneous nanosheet reaction centers during PFOS transformation, an additional batch experiment was performed under the same reaction conditions as the kinetics experiment (**Fig. 2a**). PFOS degradation by V(V)-C nanosheets were compared to degradation by vanadium oxide (i.e., V₂O₅ and V₂O₃) nanoparticle solutions (**Fig. 4b**). Upon addition of H₂O₂, PFOS defluorination efficiency increased in the order of **Blank** (i.e., PFOS only) < V₂O₃ < V₂O₅ < V(V)-C, which demonstrates that unique, synergistic and cooperative defluorination in the V(V)-C+H₂O₂ reaction system results in maximum PFOS defluorination. The PFOS removal in the V₂O₃ and V₂O₅ reaction system in the absence of H₂O₂ is believed to correspond to the physical adsorption of PFOS to trace amounts of solid V₂O₃ and V₂O₅ particles as no F⁻ release was detected. PFOS transformation does occur in the V₂O₃ and V₂O₅ systems in the presence of H₂O₂; however, it is limited by bulk-phase PFOS interactions. Furthermore, the greater defluorination extent observed in the V₂O₃ system could be due to aqueous electrochemical instabilities of dissolved V₂O₅ phases compared to V₂O₃ phases.⁷⁵ The result from this experiment suggests that the adsorption of PFOS onto heterogeneous supports in the V(V)-C system may contribute to a greater extent of defluorination than dissolved bulk-phase reaction systems. Furthermore, this test also confirms that the presence of vanadium(V) on V(V)-C nanosheets will dramatically increase PFOS transformation efficacy during the degradation process. To probe the potential reusability of V(V)-C, we observed the morphology of the V(V)-C nanosheet under SEM after reacting with H₂O₂ (**Fig. S9**). The nanosheet morphology remains, and according to the XPS results (**Fig. 3** and **Table 2**), V(V) oxidation states

within the structure still remain following the reaction. Therefore, we hypothesize that there is a possibility of reusing the V(V)-C nanosheets for subsequent cycles of treatment. Further understanding of the reusability (i.e., ways to regenerate the V(V) oxidation state of the V(V)-C) will be examined in future work.

Conclusion

Herein, we reported a novel and efficient approach for PFAS degradation in water employing oxidized V(V)-C MXene nanosheets and H₂O₂. The V(V)-C+H₂O₂ reaction system resulted in 96% of 50 µg/L PFOS removal within 4 hrs and near 100% defluorination with minimal short-chain PFAS formation. This approach is fast and efficient compared to other heterogeneous PFAS degradation studies reported in the literature, and can be performed under mild, aerobic conditions compared to typical anoxic and alkaline pH conditions needed in bulk-phase PFAS degradation. V(V)-C formed through the hydrolysis of V₂C MXene was studied as catalytic reaction centers to facilitate the degradation of adsorbed PFOS molecules which was evidenced by complementary ex situ analyses (XPS, EPR). We identified that inherent vanadium(V) phases are reduced to vanadium (III) phases within the V(V)-C nanosheet upon addition of H₂O₂ to produce solvated electrons and yield singlet oxygen reactive species. Solvated electrons and electron transfer initiate and propagate PFOS C-S and/or C-F cleavage and defluorination, while singlet oxygen is hypothesized to contribute to vanadium(V) haloperoxidase biomimetic behavior of V(V)-C—a phenomena that was recently reported in V(V)-C.⁵⁹ Ultimately, the short distances between adsorbed PFOS and the reactive species formed, coupled with the fast charge transfer kinetics and pseudocapacitive properties of the V(V)-C nanosheets enabled rapid, degradation and defluorination of a recalcitrant, acutely toxic organic contaminant.

Further research is needed to fully understand the portfolio of toxicants degraded using this heterogeneous V(V)-C catalyst approach, the aquatic conditions under which this method is most effective, the possibility of regenerating the V(V) surface via chemical or electrochemical activation, and to determine the potential for combining it with other technologies (such as selective PFAS adsorption) to optimize its effectiveness. Future studies exploring our novel V(V)-C MXene water treatment technologies will also explore its efficacy on PFAS of different chain lengths and terminal acidic groups, as well as the effect of the aqueous chemistry (pH, temperature, ionic strength, etc.) on PFAS defluorination.

Author Contributions

Y.Y. performed all EPR, XPS, LC-MS/MS and IC experiments and collected and analyzed all of the data for this work. H.B., K.D., and V.J. assisted Y.Y. in conducting batch kinetics and degradation experiments. J.M.S. performed the degradation kinetics fits with pseudo-first- and pseudo-second order reaction rate models. J.R.R. oversaw data analysis, and

personnel management and contributed to writing and mechanism formulation.

Conflicts of interest

There are no conflicts to declare.

Acknowledgments

Part of this work was conducted at the Molecular Analysis Facility, a National Nanotechnology Coordinated Infrastructure (NNCI) site at the University of Washington, which is supported in part by funds from the National Science Foundation (awards NNCI-2025489, NNCI-1542101), the Molecular Engineering & Sciences Institute, and the Clean Energy Institute. Steigerwald was supported by the National Science Foundation Graduate Research Fellowship Program under Grant No. DGE-1762114. Any opinions, findings, and conclusions or recommendations expressed in this material are those of the authors and do not necessarily reflect the views of the National Science Foundation. This work was also supported by the University of Washington start-up funds.

We would like to thank Professor William Tarphe and Ms. Jinyu Guo from Stanford University Department of Chemical Engineering for performing cyclic voltammogram experiments and subsequent analyses to probe electron transport within the as-prepared V₂C MXene powder. Professor Guozhong Cao from the University of Washington Department of Material & Science Engineering for providing vanadium oxide powders for this study. We would also like to thank Dr. Martin Sadilek from the University of Washington Department of Chemistry for assistance with PFAS quantification optimization during LC-MS/MS analysis and Lizzy Canarie from the University of Washington Department of Chemistry for EPR sample measurements.

Notes and References

- 1 Tian, H., Gao, J., Li, H., Boyd, S. A. & Gu, C. Complete defluorination of perfluorinated compounds by hydrated electrons generated from 3-indole-acetic-acid in organomodified montmorillonite. *Sci. Rep.* **6**, 32949 (2016).
- 2 Richardson, S. D. & Kimura, S. Y. Emerging environmental contaminants: Challenges facing our next generation and potential engineering solutions. *Environ. Technol. Innov.* **8**, 40-56 (2017).
- 3 Gallen, C., Eaglesham, G., Drage, D., Nguyen, T. H. & Mueller, J. A mass estimate of perfluoroalkyl substance (PFAS) release from Australian wastewater treatment plants. *Chemosphere* **208**, 975-983 (2018).
- 4 Anderko, L. & Pennea, E. Exposures to per- and polyfluoroalkyl substances (PFAS): Potential risks to reproductive and children's health. *Cur. Probl. Pediatr. Adolesc. Health Care* **50**, 100760 (2020).

- 5 Stanifer, J. W. *et al.* Perfluorinated chemicals as emerging environmental threats to kidney health: A scoping review. *Clin. J. Am. Soc. Nephro.* **13**, 1479-1492 (2018).
- 6 Blake, B. E. & Fenton, S. E. Early life exposure to per-and polyfluoroalkyl substances (PFAS) and latent health outcomes: a review including the placenta as a target tissue and possible driver of peri-and postnatal effects. *Toxicology* **443**, 152565 (2020).
- 7 Rice, P. A., Cooper, J., Koh-Fallet, S. E. & Kabadi, S. V. Comparative analysis of the physicochemical, toxicokinetic, and toxicological properties of ether-PFAS. *Toxicology and Applied Pharmacology* **422**, 115531 (2021).
- 8 Andrews, D. Q. & Naidenko, O. V. Population-wide exposure to per-and polyfluoroalkyl substances from drinking water in the United States. *Environ. Sci. Technol. Lett.* **7**, 931-936 (2020).
- 9 Appleman, T. D. *et al.* Treatment of poly-and perfluoroalkyl substances in US full-scale water treatment systems. *Water Res.* **51**, 246-255 (2014).
- 10 Xiao, F., Hanson, R. A., Golovko, S. A., Golovko, M. Y. & Arnold, W. A. PFOA and PFOS are generated from zwitterionic and cationic precursor compounds during water disinfection with chlorine or ozone. *Environmental Science & Technology Letters* **5**, 382-388 (2018).
- 11 Dhangar, K., and Manish Kumar. Perfluorooctanesulfonate (PFOS), its occurrence, fate, transport and removal in various environmental media: a review. *Contaminants in Drinking and Wastewater Sources* 405-436 (2021).
- 12 Chen, Z. *et al.* Highly efficient hydrated electron utilization and reductive destruction of perfluoroalkyl substances induced by intermolecular interaction. *Environ. Sci. Technol.* **55**, 3996-4006 (2021).
- 13 Park, H. *et al.* Reductive defluorination of aqueous perfluorinated alkyl surfactants: effects of ionic headgroup and chain length. *The Journal of Physical Chemistry A* **113**, 690-696 (2009).
- 14 Cui, J., Gao, P. & Deng, Y. Destruction of per-and polyfluoroalkyl substances (PFAS) with advanced reduction processes (ARPs): A critical review. *Environ. Sci. Technol.* **54**, 3752-3766 (2020).
- 15 Song, Z., Tang, H., Wang, N. & Zhu, L. Reductive defluorination of perfluorooctanoic acid by hydrated electrons in a sulfite-mediated UV photochemical system. *J. Hazard. Mater.* **262**, 332-338 (2013).
- 16 Gu, Y., Dong, W., Luo, C. & Liu, T. Efficient reductive decomposition of perfluorooctanesulfonate in a high photon flux UV/sulfite system. *Environ. Sci. Technol.* **50**, 10554-10561 (2016).
- 17 Qu, Y., Zhang, C., Li, F., Chen, J. & Zhou, Q. Photo-reductive defluorination of perfluorooctanoic acid in water. *Water Res.* **44**, 2939-2947 (2010).
- 18 Wang, Y. & Zhang, P. Effects of pH on photochemical decomposition of perfluorooctanoic acid in different atmospheres by 185 nm vacuum ultraviolet. *Journal of Environmental Sciences* **26**, 2207-2214 (2014).
- 19 Chen, J. *et al.* Co-NCNT nanohybrid as a highly active catalyst for the electroreduction of nitrate to ammonia. *Chemical Communications* **58**, 3787-3790 (2022).
- 20 Franke, V., Schäfers, M. D., Lindberg, J. J. & Ahrens, L. Removal of per-and polyfluoroalkyl substances (PFASs) from tap water using heterogeneously catalyzed ozonation. *Environ. Sci. Water Res.* **5**, 1887-1896 (2019).
- 21 Alvarez, P. J., Chan, C. K., Elimelech, M., Halas, N. J. & Villagrán, D. Emerging opportunities for nanotechnology to enhance water security. *Nat. Nanotechnol.* **13**, 634-641 (2018).
- 22 Tian, H. *et al.* Enhanced photoreduction of nitro-aromatic compounds by hydrated electrons derived from indole on natural montmorillonite. *Environ. Sci. Technol.* **49**, 7784-7792 (2015).
- 23 Hodges, B. C., Cates, E. L. & Kim, J. Challenges and prospects of advanced oxidation water treatment processes using catalytic nanomaterials. *Nat. Nanotechnol.* **13**, 642-650 (2018).
- 24 Shan, Q. *et al.* Two-dimensional vanadium carbide (V₂C) MXene as electrode for supercapacitors with aqueous electrolytes. *Electrochem. Commun.* **96**, 103-107 (2018).
- 25 Driscoll, N. *et al.* Two-dimensional Ti₃C₂ MXene for high-resolution neural interfaces. *ACS Nano* **12**, 10419-10429 (2018).
- 26 Huang, Z. *et al.* Two-dimensional MXene-based materials for photothermal therapy. *Nanophotonics* **9**, 2233-2249 (2020).
- 27 Pandey, R. P., Rasool, K., Abdul Rasheed, P. & Mahmoud, K. A. Reductive sequestration of toxic bromate from drinking water using lamellar two-dimensional Ti₃C₂T_x (MXene). *ACS Sustain. Chem. Eng.* **6**, 7910-7917 (2018).
- 28 Tao, N. *et al.* Near-infrared light-responsive hydrogels via peroxide-decorated MXene-initiated polymerization. *Chem. Sci.* **10**, 10765-10771 (2019).
- 29 Chen, C. *et al.* Charge transfer induced polymerization of EDOT confined between 2D titanium carbide layers. *J. Mat. Chem. A* **5**, 5260-5265 (2017).
- 30 Mashtalir, O. *et al.* Dye adsorption and decomposition on two-dimensional titanium carbide in aqueous media. *J. Mat. Chem. A* **2**, 14334-14338 (2014).
- 31 Ihsanullah, I. MXenes (two-dimensional metal carbides) as emerging nanomaterials for water purification: Progress, challenges and prospects. *Chem. Eng. J.* **388**, 124340 (2020).
- 32 Choi, D., Blomgren, G. E. & Kumta, P. N. Fast and reversible surface redox reaction in nanocrystalline vanadium nitride supercapacitors. *Adv. Mater.* **18**, 1178-1182 (2006).
- 33 Liu, B. *et al.* Extraordinary pseudocapacitive energy storage triggered by phase transformation in hierarchical vanadium oxides. *Nat. Commun.* **9**, 1-9 (2018).
- 34 Augustyn, V., Simon, P. & Dunn, B. Pseudocapacitive oxide materials for high-rate electrochemical energy storage. *Energy Environ. Sci.* **7**, 1597-1614 (2014).
- 35 Robert, K. *et al.* Novel insights into the charge storage mechanism in pseudocapacitive vanadium nitride thick films for high-performance on-chip micro-supercapacitors. *Energy Environ. Sci.* **13**, 949-957 (2020).
- 36 Aigueperse, J. *et al.* *Ullmann's Encyclopedia of Industrial Chemistry*. (Wiley-VCH, 2000).
- 37 Zhu, X. *et al.* Superior-performance aqueous zinc-ion batteries based on the in situ growth of MnO₂ nanosheets on V₂CT_x MXene. *ACS nano* **15**, 2971-2983 (2021).
- 38 Jun, B., Han, J., Park, C. M. & Yoon, Y. Ultrasonic degradation of selected dyes using Ti₃C₂T_x MXene as a sonocatalyst. *Ultraso. Sonochem.* **64**, 104993 (2020).

- 39 Clites, M. & Pomerantseva, E. Bilayered vanadium oxides by chemical pre-intercalation of alkali and alkali-earth ions as battery electrodes. *Energy Storage Materials* **11**, 30-37 (2018).
- 40 Ain, Q. T., Haq, S. H., Alshammari, A., Al-Mutlaq, M. A. & Anjum, M. N. The systemic effect of PEG-nGO-induced oxidative stress in vivo in a rodent model. *Beilstein journal of nanotechnology* **10**, 901-911 (2019).
- 41 Gagliano, E., Sgroi, M., Falciglia, P. P., Vagliasindi, F. G. & Roccaro, P. Removal of poly-and perfluoroalkyl substances (PFAS) from water by adsorption: Role of PFAS chain length, effect of organic matter and challenges in adsorbent regeneration. *Water Res.* **171**, 115381 (2020).
- 42 Becanova, J. *et al.* A graphene-based hydrogel monolith with tailored surface chemistry for PFAS passive sampling. *Environ. Sci. Nano* **8**, 2894-2907 (2021).
- 43 Mitchell, S. M., Ahmad, M., Teel, A. L. & Watts, R. J. Degradation of perfluorooctanoic acid by reactive species generated through catalyzed H₂O₂ propagation reactions. *Environ. Sci. Technol. Lett* **1**, 117-121 (2014).
- 44 Hori, H. *et al.* Decomposition of environmentally persistent perfluorooctanoic acid in water by photochemical approaches. *Environ. Sci. Technol.* **38**, 6118-6124 (2004).
- 45 Luo, Q. *et al.* Laccase-catalyzed degradation of perfluorooctanoic acid. *Environ. Sci. Technol. Lett.* **2**, 198-203 (2015).
- 46 Benjamin, M. M. & Lawler, D. F. *Water Quality Engineering: Physical/chemical Treatment Processes.* (John Wiley & Sons, 2013).
- 47 Lyu, X., Li, W., Lam, P. K. & Yu, H. Insights into perfluorooctane sulfonate photodegradation in a catalyst-free aqueous solution. *Sci. Rep.* **5**, 1-6 (2015).
- 48 Park, H. *et al.* Reductive defluorination of aqueous perfluorinated alkyl surfactants: effects of ionic headgroup and chain length. *J. Phys. Chem. A* **113**, 690-696 (2009).
- 49 Tan, X. *et al.* Revealing the molecular-level interactions between cationic fluorinated polymer sorbents and the major PFAS pollutant PFOA. *Macromolecules* **55**, 1077-1087 (2022).
- 50 Li, L. *et al.* Modulating Electron Transfer in Vanadium - Based Artificial Enzymes for Enhanced ROS - Catalysis and Disinfection. *Advanced Materials* **34**, 2108646 (2022).
- 51 Andris, R., Averianov, T. & Pomerantseva, E. Phase transformation and electrochemical charge storage properties of vanadium oxide/carbon composite electrodes synthesized via integration with dopamine. *Journal of the American Ceramic Society* (2022).
- 52 Liu, F. *et al.* Prelithiated V₂C MXene: A High-Performance Electrode for Hybrid Magnesium/Lithium-Ion Batteries by Ion Cointercalation. *Small* **16**, 1906076 (2020). [https://doi.org:https://doi.org/10.1002/sml.201906076](https://doi.org/10.1002/sml.201906076)
- 53 Biesinger, M. C., Lau, L. W., Gerson, A. R. & Smart, R. S. C. Resolving surface chemical states in XPS analysis of first row transition metals, oxides and hydroxides: Sc, Ti, V, Cu and Zn. *Appl. Surf. Sci.* **257**, 887-898 (2010).
- 54 Wang, Z., Liu, J., Du, Z., Tao, H. & Yue, Y. Enhancing Na-ion storage in Na₃V₂(PO₄)₃/C cathodes for sodium ion batteries through Br and N co-doping. *Inorg. Chem. Front.* **7**, 1289-1297 (2020).
- 55 Silversmit, G., Depla, D., Poelman, H., Marin, G. B. & De Gryse, R. Determination of the V2p XPS binding energies for different vanadium oxidation states (V⁵⁺ to V⁰⁺). *J. Electron. Spectros. Relat. Phenomena* **135**, 167-175 (2004).
- 56 Naguib, M. *et al.* New two-dimensional niobium and vanadium carbides as promising materials for Li-ion batteries. *J. Am. Chem. Soc.* **135**, 15966-15969 (2013).
- 57 Chastain, J. & King Jr, R. C. Handbook of X-ray photoelectron spectroscopy. *Perkin-Elmer Corporation* **40**, 221 (1992).
- 58 Yang, C. *et al.* V₅S₈-graphite hybrid nanosheets as a high rate-capacity and stable anode material for sodium-ion batteries. *Energy Environ. Sci.* **10**, 107-113 (2017).
- 59 Feng, W. *et al.* 2D vanadium carbide MXene to alleviate ROS-mediated inflammatory and neurodegenerative diseases. *Nat. Commun.* **12**, 1-16 (2021).
- 60 Bai, L. *et al.* Response to Comment on "Mechanistic Understanding of Superoxide Radical-Mediated Degradation of Perfluorocarboxylic Acids". *Environmental Science & Technology* **56**, 5289-5291 (2022).
- 61 Colpas, G. J., Hamstra, B. J., Kampf, J. W. & Pecoraro, V. L. Functional models for vanadium haloperoxidase: reactivity and mechanism of halide oxidation. *J. Am. Chem. Soc.* **118**, 3469-3478 (1996).
- 62 Moriawaki, H. *et al.* Sonochemical decomposition of perfluorooctane sulfonate and perfluorooctanoic acid. *Environ. Sci. Tech.* **39**, 3388-3392 (2005).
- 63 Vesel, A., Mozetic, M. & Zalar, A. XPS characterization of PTFE after treatment with RF oxygen and nitrogen plasma. *Surf. Interface Anal.* **40**, 661-663 (2008).
- 64 Tokranov, A. K. *et al.* How do we measure poly-and perfluoroalkyl substances (PFASs) at the surface of consumer products? *Environ. Sci. Technol. Lett.* **6**, 38-43 (2018).
- 65 Suthersan, S. S. *et al.* Responding to emerging contaminant impacts: Situational management. *Ground Water Monit. Remediat.* **36**, 22-32 (2016).
- 66 Bell, R., Zemski, K. & Castleman, A. Gas-phase chemistry of vanadium oxide cluster cations. 2. Reactions with CH₂F₂. *The Journal of Physical Chemistry A* **103**, 2992-2998 (1999).
- 67 Levason, W., Monzittu, F. M. & Reid, G. Coordination chemistry and applications of medium/high oxidation state metal and non-metal fluoride and oxide-fluoride complexes with neutral donor ligands. *Coordination Chemistry Reviews* **391**, 90-130 (2019).
- 68 Kiplinger, J. L., Richmond, T. G. & Osterberg, C. E. Activation of carbon-fluorine bonds by metal complexes. *Chem. Rev.* **94**, 373-431 (1994).
- 69 Harrison, R. G. & Richmond, T. G. Reductive defluorination of saturated perfluorocarbons by organometallic nucleophiles. *J. Am. Chem. Soc.* **115**, 5303-5304 (1993).
- 70 Wang, Z. *et al.* VO₂ (p)-V₂C (MXene) grid structure as a lithium polysulfide catalytic host for high-performance Li-S battery. *ACS Appl. Mater. Interfaces* **11**, 44282-44292 (2019).
- 71 Roznyatovskaya, N., Noack, J., Pinkwart, K. & Tübke, J. Aspects of electron transfer processes in vanadium redox-flow batteries. *Curr. Opin. Electrochem.* **19**, 42-48 (2020).
- 72 Liu, F. *et al.* Prelithiated V₂C MXene: A High-performance electrode for hybrid magnesium/lithium-ion batteries by

ARTICLE

Journal Name

- ion cointercalation. *Small* **16**, 1906076 (2020).
- 73 Cui, J., Gao, P. & Deng, Y. Destruction of per-and polyfluoroalkyl substances (PFAS) with advanced reduction processes (ARPs): A critical review. *Environ. Sci. Technol.* **54**, 3752-3766 (2020).
- 74 Gu, Y., Liu, T., Wang, H., Han, H. & Dong, W. Hydrated electron based decomposition of perfluorooctane sulfonate (PFOS) in the VUV/sulfite system. *Science of the Total Environment* **607**, 541-548 (2017).
- 75 Lu, Y., Zhu, T., van den Bergh, W., Stefik, M. & Huang, K. A high performing Zn - ion battery cathode enabled by in situ transformation of V₂O₅ atomic layers. *Angew. Chem. Int* **59**, 17004-17011 (2020).